Journal of Physics D: Applied Physics

PAPER

Underwater acoustic multiplexing communication by pentamode metasurface

To cite this article: Zhaoyong Sun *et al* 2021 *J. Phys. D: Appl. Phys.* **54** 205303

IOP Publishing Journal of Physics D: Applied Physics
J. Phys. D: Appl. Phys. **54** (2021) 205303 (7pp) https://doi.org/10.1088/1361-6463/abe43e

Underwater acoustic multiplexing communication by pentamode metasurface

Zhaoyong Sun[1,5], Yu Shi[2,5], Xuecong Sun[1,3], Han Jia[3,4], Zhongkun Jin[1], Ke Deng[2] and Jun Yang[1,3]

[1] Key Laboratory of Noise and Vibration Research, Institute of Acoustics, Chinese Academy of Sciences, Beijing 100190, People's Republic of China
[2] Department of Physics, Jishou University, Jishou 416000, Hunan, People's Republic of China
[3] University of Chinese Academy of Sciences, Beijing 100049, People's Republic of China
[4] State Key Laboratory of Acoustics, Institute of Acoustics, Chinese Academy of Sciences, Beijing 100190, People's Republic of China

E-mail: hjia@mail.ioa.ac.cn, dengke@jsu.edu.cn and jyang@mail.ioa.ac.cn

Received 9 December 2020, revised 20 January 2021
Accepted for publication 8 February 2021
Published 1 March 2021

Abstract

As the dominant information carrier in water, the acoustic wave is widely used for underwater detection, communication and imaging. Even though underwater acoustic communication has been greatly improved in the past decades, it still suffers from slow transmission speeds and low information capacity. The recently developed acoustic orbital angular momentum (OAM) multiplexing communication promises a high efficiency, large capacity and fast transmission speed for acoustic communication. However, the current works on OAM multiplexing communication mainly appear in airborne acoustics. The application of acoustic OAM for underwater communication remains to be further explored and studied. In this paper, an impedance matching pentamode demultiplexing metasurface is designed to realize multiplexing and demultiplexing in underwater acoustic communication. The impedance matching of the metasurface ensures high transmission of the transmitted information. The information encoded into two different OAM beams as two independent channels is numerically demonstrated by realizing real-time picture transfer. The simulation shows the effectiveness of the system for underwater acoustic multiplexing communication. This work paves the way for experimental demonstration and practical application of OAM multiplexing for underwater acoustic communication.

Supplementary material for this article is available online

Keywords: orbital angular momentum, multiplexing communication, pentamode, acoustic metasurface

(Some figures may appear in colour only in the online journal)

The ocean, which accounts for 75% of the earth's area, contains rich resources and mysterious species. Therefore, it is extremely important for human beings to understand, explore and develop the ocean. Underwater communication technology is an important approach for ocean exploration. However, light and electromagnetic waves decay easily in water so they are difficult to use for underwater detection. The acoustic wave does not attenuate and is not scattered easily in water, thus it is the major carrier of underwater information and can be used to realize underwater communication and imaging. There are problems of low frequency and low

[5] These authors contributed equally.

speed based on acoustic communication, which do not meet the growing demand of data transmission. How to improve the transmission speed and expand the information capacity of acoustic communication is an urgent problem. Acoustic orbital angular momentum (OAM) provides a feasible scheme to solve this problem.

The OAM is carried by the vortex wave, which has been widely studied and applied in the context of optics and electromagnetic waves [1–7]. The equiphase surface of the vortex wave shows the shape of a spiral, where the rotation rate is mainly described by the OAM order (also named as topological charge). This leads to a doughnut-shaped intensity profile. These characteristics provide an additional freedom that allows the vortex wave to have more application prospects, for example, optical OAM beams have found significant applications from objects manipulation [8, 9] to imaging [10] and multiplexing communications [11–15].

Due to the similarity between optics and acoustics, OAM in acoustics has been investigated extensively in recent decades. Many efforts on acoustic vortex waves have been reported, including OAM beam formed by active arrays [16] and metamaterials [17–21], OAM beams used for object manipulation [22–27], acoustic analogy of the supper radiance of Kerr black holes [28, 29] etc. Additionally, acoustic OAM used for communication is also one of the most attractive topics. The first attempt in acoustic OAM communication was realized using a transducer array in air [30]. An orthogonal acoustic vortex beam was created by the designed active array to provide more physical channels for information transmission. An active sensor array was set on the receiving end to scan the acoustic field and the information was demultiplexed by an inner product algorithm. Thus, the transmission speed was limited by the sensor scanning and postprocess. In order to overcome these issues, a passive, postprocess-free and sensor scanning-free OAM communication system was designed with airborne based demultiplexing metasurfaces (DMMs) [31], where the OAM could be lowered by 1 after passing through a DMM. In the system, the information was compiled into different OAM beams, where each beam was an independent channel. Considering the doughnut-shaped intensity profile of OAM beam and the fact that the spiral phase of mth OAM beam can only be eliminated after passing through the mth metasurface, the encoded information can be immediately decoded by the DMM with a microphone in the center behind each metasurface.

Due to the crucial role of acoustics in underwater circumstances, OAM multiplexing technology can be used to improve the efficiency of underwater communication. Although there are some works to attempt to utilize OAM in airborne acoustic communication [30–33], the application of OAM in underwater multiplexing communication remains to be further developed [18, 34].

One way to provide OAM multiplexing in underwater communication is to extend the DMM system [31] to the underwater case. However, one of the biggest challenges for an underwater metasurface is the difficulty of impedance matching. A suitable approach is using a pentamode material (PM), which is fabricated from rigid solids (usually with metal) but exhibits fluid-like acoustic properties [35–40].

In the two-dimensional (2D) condition, PM is realized by a hexagonal lattice structure. The shear modulus of the latticed PM is small enough that it can be neglected and regarded as fluid in some frequency bands. The effective acoustic properties can be effectively adjusted by tuning the geometric parameters, for example, it can be designed to have anisotropic or isotropic modulus [41, 42]. This property has meant that PMs have been widely studied and applied in underwater acoustic wave control [43–54].

In this paper, we use a 2D latticed PM to design an impedance matching underwater acoustic demultiplexing metasurface (PM-DMM) with thickness of 0.19λ and radius of 0.44λ (λ denoted as sound wavelength). With such a PM-DMM, a passive, postprocess-free and sensor scanning-free OAM-based underwater acoustic multiplexing communication system is constructed, which can decode data directly and promptly by using two transducers. In the simulation, the information is encoded by mixing the plane wave and 1st order OAM beam together, where each of them carries a part of the information. Taking full advantage of the intensity profile of the OAM beam, the information carried by the 1st order beam can be detected with the probe placed at the back of the PM-DMM, while the other information in the plane wave can be detected with the probe located in front of the PM-DMM. The simulation shows the effectiveness of the system for underwater acoustic multiplexing communication.

In the cylindrical coordinates system (denoted as r, θ, z), the pressure field of the mth order acoustic OAM beam is expressed as:

$$P = A_m(r,t)e^{i(kz+m\theta+\phi_m(t))}, \tag{1}$$

where $A_m(r,t)$ and $\phi_m(t)$ are the time dependent amplitude and phase, respectively. The index m, also named the topological charge, indicates the order of the OAM. From equation (1), it can be seen that the wavefront rotates around z with the speed of $m \times 2\pi$ per revolution. The sign of the topological charge indicates direction of wavefront rotation, i.e. a plus sign means rotating in anticlockwise direction, while the minus sign corresponds to a clockwise rotation. The beam with $m = 0$ represents the plane wave, while the one with $m = \pm 1$ has a continuos spiral shaped wavefront which leads to the zero pressure at the central axis.

From equation (1), it is easy to see that the vortex waves with different OAM orders are orthogonal [33], thus these OAM beams can be used as orthogonal channels to realize multiplexing communication. The information capacity can be increased by N times for the signal with N vortex waves with different OAM orders.

Since a well designed OAM metasurface can increase or decrease the order of the vortex wave that passes through it [31], the OAM of a mth order beam can be lowered to $m - n$ after n identical -1 valued OAM metasurfaces. This promises a metasurface based passive DMM system. The mechanism is very intuitive: encoding the information into the vortex waves

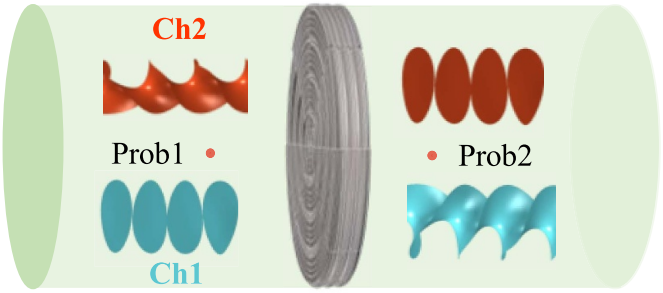

Figure 1. Schematic representation of DMM based multiplexing communication system.

in advance and taking advantage of the null pressure at central axis, one can obtain the amplitude and phase of the nth order vortex wave by placing a detection point at the central axis behind the nth metasurface. Figure 1 illustrates the working principle of the DMM composed of one OAM metasurface. The DMM connects with two cylindrical waveguides, where two probes are set at the center in front of (probe 1) and behind (probe 2) the metasurface. The multiplexing signal composed of plane wave and 1st order OAM wave is emitted from the left end. The plane wave in the multiplexing signal is denoted as the first channel (Ch1), while the 1st OAM beam as the second channel (Ch2). The metasurface can reduce the OAM of the incident wave by 1 order. Thus the plane wave is converted to -1st OAM beam, while the 1st OAM beam is reduced to the plane wave. Because of the null pressure at the central axis in the OAM beams, probe i can only read the information in Chi ($i = 1, 2$), as shown in figure 1.

The mth order OAM metasurface of thickness l should be designed by the fact that the phase difference at the two surfaces of the metasurface is in a linear correlation with θ [31]:

$$\varphi_{\text{output}} - \varphi_{\text{input}} = m\theta + \theta_0 = kl, \tag{2}$$

where k is the wave vector in the metasurface and θ_0 is a constant. Thus, it is obvious that the velocity distribution $c(\theta)$ is:

$$c(\theta) = \frac{2\pi fl}{m\theta + \theta_0}. \tag{3}$$

From equation (3), it is easy to see that the refractive index of the metasurface varies gradiently with θ. Considering the impedance matching condition, the non-dimensional density and bulk modulus can be immediately derived as:

$$\rho = \frac{m\theta + \theta_0}{2\pi fl} c_0, \tag{4a}$$

$$K = \frac{2\pi fl}{(m\theta + \theta_0)c_0}, \tag{4b}$$

where the dimensionless parameters are obtained through dividing the normal density and modulus by the corresponding values of background media. c_0 in equation (4b) is the acoustic velocity in the background media. Such a metasurface can be used for passive multiplexing communication.

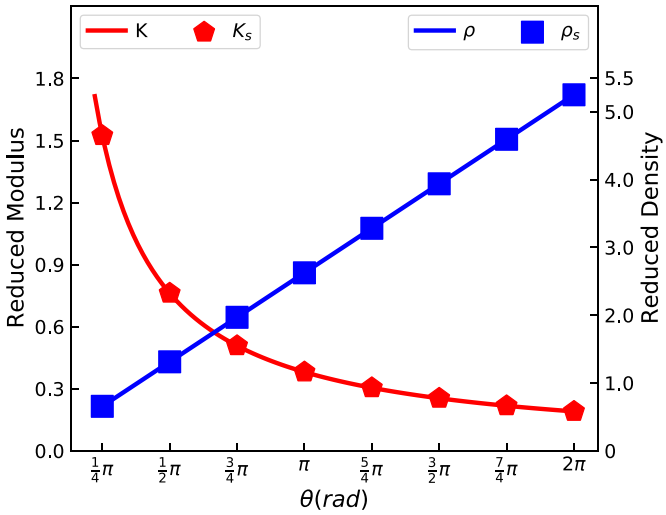

Figure 2. The distributions of the bulk modulus and density of the PM-DMM. The profiles of continuously varying acoustic parameters(modulus K marked by red solid line and density ρ marked by blue solid line) and the corresponding discrete parameters(modulus K_s by red pentagon and density ρ_s by blue squares).

The designed metasurface is a flat column with thickness $l = 40$ mm and radius $r = 92.38$ mm. The constant θ_0, which is used to adjust the density and modulus, is chosen as 0 here. The distributions of ρ and K along the θ direction are shown in figure 2, marked by red and blue lines correspondingly.

It's clear that the density increases with θ linearly, while the bulk modulus decreases inversely with θ. In order to realize the metasurface with metamaterials, the designed metasurface is pre-divided into eight equal sectors with central angle of $\pi/4$. Then, the continued parameters, density ρ and bulk modulus K, are discretized into eight discrete groups which are marked by blue squares (density) and red pentagons (modulus).

Since PM is excellent in underwater acoustic wave control [44–51], we use it to construct the designed metasurface.

Figure 3 shows the energy bands of the latticed PM. The geometry of the unit cell is shown in figure 3(b), where the yellow colored equilateral triangles are the additional mass blocks only used in the third sector. In the quasi-static regime, such a hexagonal lattice can exhibit properties similar to isotropic fluids. The effective acoustic properties of the latticed PM are mainly determined by the geometric parameters, which are characterized by side length l, structure thickness t, block size (w, h), additional block size (the yellow colored triangles in figure 3(b)) and corner factor q that are shown in figure 3(c). Figure 3(a) shows the the first six bands of the unit cell used in the second sector. At the quasi-static regime [55], the effective density of PM equals the volume average of the cell mass. The longitudinal and shear wave velocities can be obtained from the band diagram directively. Thus, the effective acoustic properties can be obtained by retrieving the energy bands [44, 50], which is different from the standard retrieval method [56]. According to the discrete parameters in figure 2, the eight needed unitcells are obtained from the energy bands retrieval method [44, 50]. The basis material for the unit cells in the

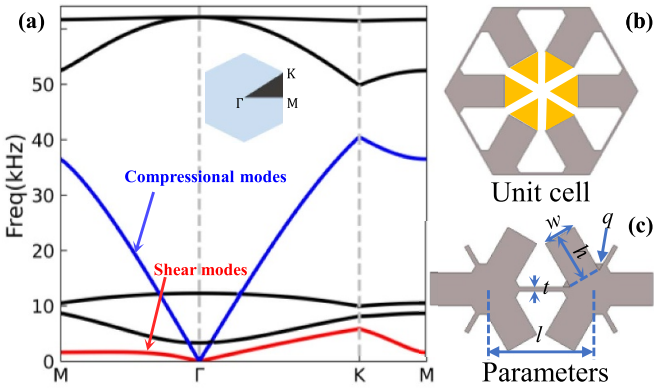

Figure 3. Band diagram (a) of the unit cell (b) with the parameters names shown as (c).

first three sectors is aluminum with $E = 69$ GPa, $\sigma = 0.33$ and $\rho = 2700$ kg m^{-3}, while that for the last five sectors is lead with $E = 16.4$ GPa, $\sigma = 0.44$ and $\rho = 11400$ kg m^{-3}. Therefore, E, σ and ρ represent the Young's modulus, Poisson's ratio and density, respectively. The background media is water with density of $\rho_0 = 1000$ kg m^{-3} and bulk modulus of $K_0 = 2.25$ GPa. The side length of the cells are $l = 7.70$ mm, while the corner factor is an equilateral triangle with side length of 1.15 mm. The dimensionless thickness $t2l$ and dimensionless block size$(w_{\rm rat}, h_{\rm rat})$ are calculated as t/l and $(w/l, h/l)$, respectively. The geometry parameters and effective properties of the PM unit cells are shown in table 1. In order to increase the density of the third structure, additional mass blocks are added to the mass blocks, and the corner factors are excluded.

With careful tailoring, the eight rectangle-like structures are constructed and shown in figure 4(b), which are the corresponding $r-z$ cross-sections of the eight sectors. In order to evaluate the properties, the performance, i.e. transmission and phase shifts, of the eight structures are simulated using the COMSOL Multiphysics software. The simulation is finished in a waveguide tube shown in figure 4(c), where the waves at the frequency of 7100 Hz are incident from left. The structures in figure 4(c) are the ones exactly in figure 4(b). From figure 4(c), it is clear that the transmitted phases of the eight structures vary gradiently. A more accurate evaluation of the phase shift is shown in figure 4(d) marked by blue squares. The phase shift varies from 0.38π at sector 1 to -0.83π at sector 6, jumps to 0.90π at sector 7 and declines to 0.66π at sector 8. Apparently, the phase shift satisfies the relationship in equation (2). The high transmission, marked by red triangles in figure 4(d), implies good impedance matching performance of the structures. The final PM-DMM, as shown in figure 4(a), can be constructed by rotating the eight rectangle-like structures around the z-axis by $\pi/4$.

In order to verify the effectiveness of the OAM metasurface, the performance of the PM-DMM is simulated in a waveguide by the finite element solver COMSOL Multiphysics. In the simulation, the PM-DMM is placed in the center of a cylindrical acoustic waveguide with a length of 1500 mm and a radius of 92.38 mm, which is exactly the same as the radius of the metasurface. The center point of the PM-DMM is set

Table 1. Geometric parameters and effective properties of the PM unitcells.

No.	$\rho_{\rm eff}$	$\kappa_{\rm eff}$	$t2l$	$w_{\rm rat}$	$h_{\rm rat}$
1	0.6558	1.5248	0.0900	0.3194	0.1308
2	1.3116	0.7624	0.0428	0.3346	0.5026
3	1.9674	0.5083	0.0241	0.3000	0.2923
4	2.6232	0.3812	0.0854	0.3787	0.0857
5	3.2790	0.3050	0.0803	0.2852	0.2410
6	3.9349	0.2541	0.0746	0.2160	0.4693
7	4.5907	0.2178	0.0485	0.3687	0.3417
8	5.2465	0.1906	0.0425	0.3652	0.4221

as the origin of the cylindrical coordinates. A plane wave at the frequency of 7100 Hz is emitted from the left end to the metasurface. The simulation results are shown in figure 5. In figure 5(a), it can be seen that when the plane wave passes through the metasurface, the wave front changes from planes to anti-clockwise rotating spiral surfaces, which is the characteristics of the -1st OAM beam. In addition, the amplitude and phase distributions of the -1st order vortex wave at $z = 235$ mm are obtained and shown in figures 5(b) and (c), respectively. The amplitude shows a doughnut-shaped distribution (figure 5(b)), while the phase distribution is characterized by a circumferential gradient (figure 5(c)). The yellow circle in figure 5(c) is a cut line at $r = 80$ mm, along which the phase distribution is extracted to exactly demonstrate the phase shift. The phase shift along the cut line is shown in figure 5(d). Obviously, the phase shift varies gradually between $-\pi$ and π if the periodic mutation is ignored. These results further confirm the OAM characteristics of the transmitted wave. This proves that the designed PM-DMM can lower the OAM values of the incident wave by 1 order. The distributions of the amplitude and phase imply good performance of the metasurface. Thus, it can be used for demultiplexing in underwater acoustic multiplexing communication.

We use the time domain simulation to demonstrate the multiplexing and demultiplexing of the PM-DMM in real-time underwater acoustic communication. The multiplexing signal is a superposition of the plane wave (0th OAM beam) and 1st OAM beam, where the two waves are regarded as channel 1 (Ch1) and channel 2 (Ch2), respectively. Two probes, denoted as probe 1 and probe 2, are set on the central axis in front of and behind the metasurface, respectively. A detailed schematic image is shown in figure 1. According to the analysis in the last section, the plane wave in the multiplexing signal will be converted to a -1st OAM beam after passing through the PM-DMM, while the 1st OAM beam in the multiplexing signal will be converted to a 0th OAM beam (plane wave). Consequently, the multiplexing signal can be demultiplexed by the metasurface. Detailed examples of demultiplexing can be found in the supplementary materials (available online at stacks.iop.org/JPD/54/205303/mmedia).

In this work, we simultaneously use the binary amplitude shift keying (BASP) and binary phase shift keying (BPSK) formats to encode the information. The two different amplitudes in the multiplexing signal, i.e. normalized amplitudes of 1 and 0.5, encode the 0 and 1 of binary digits, respectively.

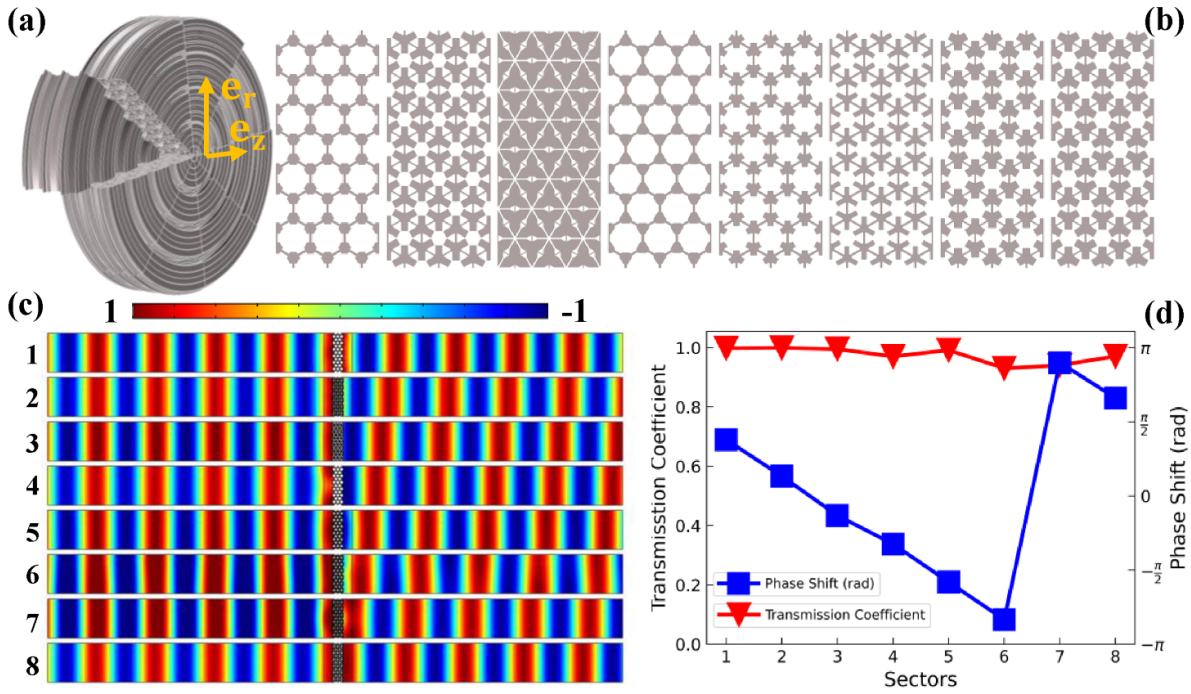

Figure 4. (a) The PM-DMM constructed by eight sectors. (b) The $r-z$ cross sections of the eight sectors. (c) Simulated sound transmission field through the eight cells. (d) The transmission coefficients (marked by red triangles) and the phase shifts (marked by blue squares) of the eight cells.

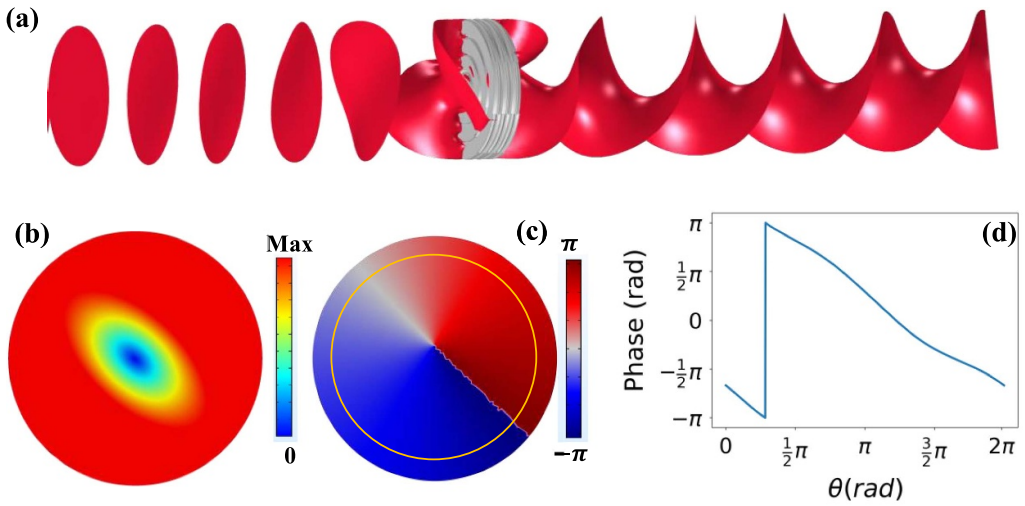

Figure 5. The simulated performance of the PM-DMM. (a) A plane wave at 7100 Hz is converted to -1st order OAM beam after passing through the PM-DMM. (b) The pressure distribution of the -1st order OAM beam at $z=235$ mm. (c) The phase distribution of the -1st order OAM beam at $z=235$ mm. (d) Phase shift along the yellow circle shown in (c) with $r=80$ mm.

In addition to amplitude modulation, phase modulation is also used to increase the information capacity, in which the 0 and 1 of the binary are represented by the two different carrier phases that are π degrees apart from each others, respectively. In such a way, the data can be encoded into the two channels of the multiplexed signal to transmit information. At the receiving end, the multiplexing signal can be demultiplexed by the PM-DMM. Thus the data encoded in different channels can be restored easily.

In the simulation of the acoustic OAM multiplexing communication, we encode every pixel in the images of letter 'IOA' into the amplitude and phase of the waves. The incident multiplexing signal is in pulse modulation denoted by $\Sigma_m p_0(T_0)e^{i(\omega t+m\theta+\phi_0(T_0))}$, in which T_0 is the period at $f_0=7100$ Hz. The pulse cycle in each channel is set as $20T_0$ with duty ratio of 0.75, where each cycle contains $2bits$ data that correspond to two pixels of the images. The amplitude and the phase in the incident signal are shown as the four

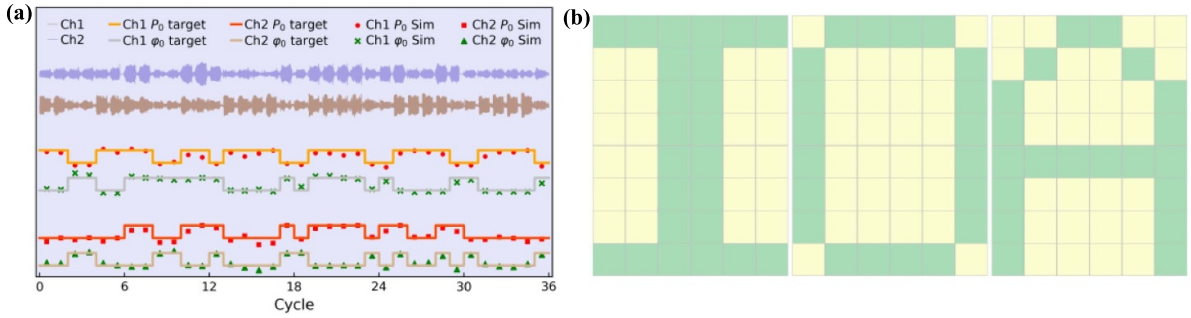

Figure 6. Multiplexing communication with signal merged in plane wave (Ch1) and 1st order OAM beam (Ch2). (a) The received signals corresponding to the letters 'IOA'. (b) Images independently retrieved from the received data carried by the two channels.

rectangular lines in figure 6(a) to be regarded as the objective data. The orange and silver lines correspond to the initial amplitude and phase in Ch1, respectively, while the orange-red and tan lines describe the amplitude and phase in Ch2 correspondingly. The detected signals in the receiving end are shown as the saddle brown line (Ch1) and slate blue line (Ch2) in figure 6(a), respectively. The distributions of the amplitude and phase in the two signals are obtained by Fourier transform and shown as the points with different symbols in figure 6(a). It can be seen that the received data is in good agreement with the objective data. This is sufficient to show that the designed PM-DMM can separate the vortex waves with different OAMs to achieve the demultiplexing. The received data shown in figure 6(a) is transformed to binary format, where the binary information 0 and 1 represent two different colors of each pixel. Thus, the images are reconstructed as shown in figure 6(b), which undistortedly form the pictures of letters 'IOA'. The detailed process of the image reconstruction can be found in the supplementary materials.

In conclusion, we have proposed and demonstrated a metasurface based passive demultiplexing system for underwater acoustic communication. This system makes good use of the characteristic of null pressure at the central axis in the OAM beam to separate different OAM beams to demultiplex the signal. This allows the system to be scanning free and post-processing free. The metasurface, used for demultiplexing, is constructed using a PM metafluid which is easy to impedance match with water, and is used for decoding with two probes before and after it. In the simulation, the 0th and 1st order OAM beams are used as two independent channels to carry data. The simulation results show the effectiveness of the system for underwater acoustic multiplexing communication. The mechanism of the demultiplexing system is not limited by the numbers of channels so a multiplexing communication with more channels can be realized by adding more metasurfaces with equal numbers of transducers. Thus, the information capacity can be expanded to be large enough for any purpose. Moreover, the simulation in this paper provides a solid theoretical reference for the experimental exploration and practical application of underwater acoustic OAM multiplexing communication.

Acknowledgements

This work is partly supported by the National Natural Science Foundation of China (Grant Nos. 11874383, 11964011, 11764016), the Youth Innovation Promotion Association CAS (Grant No. 2017029), the IACAS Young Elite Researcher Project (Grant No. QNYC201719) and Key-Area Research and Development Program of Guangdong Province (Grant No. 2020B010190002).

ORCID iD

Zhaoyong Sun https://orcid.org/0000-0001-9102-3758

References

[1] Sroor H *et al* 2020 *Nat. Photon.* **14** 498–503
[2] Wang B *et al* 2020 *Nat. Photon.* **14** 623–8
[3] Zhang Z *et al* 2020 *Science* **368** 760
[4] Ge L 2020 *Science* **368** 707
[5] Guo Y, Pu M, Zhao Z, Wang Y, Jin J, Gao P, Li X, Ma X and Luo X 2016 *ACS Photonics* **3** 2022–9
[6] Pu M *et al* 2015 *Sci. Adv.* **1** e1500396
[7] Zhang Y B, Liu H, Cheng H, Tian J G and Chen S Q 2020 *Opto-Electron. Adv.* **3** 200002
[8] Liu W, Dong D S, Yang H, Gong Q H and Shi K B 2020 *Opto-Electron. Adv.* **3** 200022
[9] Padgett M and Bowman R 2011 *Nat. Photon.* **5** 343
[10] Zhao Q, Yu P-P, Liu Y-F, Wang Z-Q, Li Y-M and Gong L 2020 *Appl. Phys. Lett.* **116** 181101
[11] Gibson G, Courtial J, Padgett M J, Vasnetsov M, Pas'ko V, Barnett S M and Franke-Arnold S 2004 *Opt. Express* **12** 5448
[12] Nagali E, Sciarrino F, De Martini F, Marrucci L, Piccirillo B, Karimi E and Santamato E 2009 *Phys. Rev. Lett.* **103** 013601
[13] Wang J *et al* 2012 *Nat. Photon.* **6** 488
[14] Bozinovic N, Yue Y, Ren Y, Tur M, Kristensen P, Huang H, Willner A E and Ramachandran S 2013 *Science* **340** 1545
[15] Wang J 2019 *Sci. China-Phys. Mech. Astron.* **62** 34201
[16] Hefner B T and Marston P L 1999 *J. Acoust. Soc. Am.* **106** 3313
[17] Jiang X, Li Y, Liang B, Cheng J and Zhang L 2016 *Phys. Rev. Lett.* **117** 034301
[18] Jiang X, Zhao J, Liu S, Liang B, Zou X, Yang J, Qiu C-W and Cheng J 2016 *Appl. Phys. Lett.* **108** 203501

[19] Jiang X, Ta D and Wang W 2020 *Phys. Rev. Appl.* **14** 034014
[20] Fu Y, Shen C, Zhu X, Li J, Liu Y, Cummer S A and Xu Y 2020 *Sci. Adv.* **6** eaba9876
[21] Ye L, Qiu C, Lu J, Tang K, Jia H, Ke M, Peng S and Liu Z 2016 *AIP Adv.* **6** 085007
[22] Zhang R, Guo H, Deng W, Huang X, Li F, Lu J and Liu Z 2020 *Appl. Phys. Lett.* **116** 123503
[23] Sanchez-Padilla B and Brasselet E 2020 *Phys. Rev. Appl.* **13** 064069
[24] Marzo A, Seah S A, Drinkwater B W, Sahoo D R, Long B and Subramanian S 2015 *Nat. Commun.* **6** 8661
[25] Gong Z and Baudoin M 2019 *Phys. Rev. Appl.* **12** 024045
[26] Zhang L 2018 *Phys. Rev. Appl.* **10** 034039
[27] Guo S, Guo X, Wang X, Du X, Wu P, Bouakaz A and Wan M 2020 *Phys. Rev. Appl.* **13** 034009
[28] Faccio D and Wright E M 2019 *Phys. Rev. Lett.* **123** 044301
[29] Cromb M, Gibson G M, Toninelli E, Padgett M J, Wright E M and Faccio D 2020 *Nat. Phys.* **16** 1069–73
[30] Shi C, Dubois M, Wang Y and Zhang X 2017 *Proc. Natl Acad. Sci. USA* **114** 7250
[31] Jiang X, Liang B, Cheng J-C and Qiu C-W 2018 *Adv. Mater.* **30** 1800257
[32] Jiang X, Shi C, Wang Y, Smalley J, Cheng J and Zhang X 2020 *Phys. Rev. Appl.* **13** 014014
[33] Li Z, Qu F, Wei Y, Yang G, Xu W and Xu J 2020 *Sci. Rep.* **10** 5216
[34] Zou Z, Lirette R and Zhang L 2020 *Phys. Rev. Lett.* **125** 074301
[35] Milton G W and Cherkaev A V 1995 *J. Eng. Mater. Technol.* **117** 483
[36] Cai X, Wang L, Zhao Z, Zhao A, Zhang X, Wu T and Chen H 2016 *Appl. Phys. Lett.* **109** 131904
[37] Cai C, Wang Z, Chu Y, Liu G and Xu Z 2017 *J. Phys. D: Appl. Phys.* **50** 415105
[38] Li Q and Vipperman J S 2019 *J. Acoust. Soc. Am.* **145** 1372
[39] Li Q and Zhang M 2020 *J. Phys.: Condens. Matter.* **32** 475701
[40] Cai C, Guo R, Wang X, Sun F, Wang Z and Xu Z 2020 *J. Appl. Phys.* **127** 124903
[41] Kadic M, Bückmann T, Stenger N, Thiel M and Wegener M 2012 *Appl. Phys. Lett.* **100** 191901
[42] Layman C N, Naify C J, Martin T P, Calvo D C and Orris G J 2013 *Phys. Rev. Lett.* **111** 024302
[43] Norris A N 2009 *J. Acoust. Soc. Am.* **125** 839
[44] Chen Y, Liu X and Hu G 2015 *Sci. Rep.* **5** 15745
[45] Chen Y, Liu X and Hu G 2016 *J. Acoust. Soc. Am.* **140** EL405
[46] Chen Y, Zheng M, Liu X, Bi Y, Sun Z, Xiang P, Yang J and Hu G 2017 *Phys. Rev.* B **95** 180104(R)
[47] Chen Y and Hu G 2019 *Phys. Rev. Appl.* **12** 044046
[48] Tian Y, Wei Q, Cheng Y, Xu Z and Liu X 2015 *Appl. Phys. Lett.* **107** 221906
[49] Su X, Norris A N, Cushing C W, Haberman M R and Wilson P S 2017 *J. Acoust. Soc. Am.* **141** 4408
[50] Sun Z, Jia H, Chen Y, Wang Z and Yang J 2018 *J. Acoust. Soc. Am.* **143** 1029
[51] Sun Z, Sun X, Jia H, Bi Y and Yang J 2019 *Appl. Phys. Lett.* **114** 094101
[52] Lu Z-M, Cai L, Wen J-H and Chen X 2019 *Chin. Phys. Lett.* **36** 024301
[53] Nie X, Chen Y and Liu X 2020 *Acta Mech. Solida Sin.* **33** 347
[54] Yu R, Wang H, Chen W, Zhu C and Wu D 2020 *Appl. Phys. Express* **13** 084003
[55] Norris A 2014 *Proc. R. Soc.* A **470** 20140522
[56] Zhao L, Laredo E, Ryan O, Yazdkhasti A, Kim H-T, Ganye R, Horiuchi T and Yu M 2020 *Appl. Phys. Lett.* **116** 071902